J. Fluid Mech. (2011), *vol.* 688, *pp.* 31–43.
doi:10.1017/jfm.2011.354

Prandtl and Rayleigh number dependence of heat transport in high Rayleigh number thermal convection

Richard J. A. M. Stevens[1]†, Detlef Lohse[1] and Roberto Verzicco[1,2]

[1] Department of Science and Technology and J.M. Burgers Center for Fluid Dynamics, University of Twente, PO Box 217, 7500 AE Enschede, The Netherlands

[2] Department of Mechanical Engineering, Universitá di Roma 'Tor Vergata', Via del Politecnico 1, 00133, Roma

(Received 11 April 2011; revised 13 June 2011; accepted 18 August 2011; first published online 24 October 2011)

Results from direct numerical simulation for three-dimensional Rayleigh–Bénard convection in samples of aspect ratio $\Gamma = 0.23$ and $\Gamma = 1/2$ up to Rayleigh number $Ra = 2 \times 10^{12}$ are presented. The broad range of Prandtl numbers $0.5 < Pr < 10$ is considered. In contrast to some experiments, we do not see any increase in $Nu/Ra^{1/3}$ with increasing Ra, neither due to an increasing Pr, nor due to constant heat flux boundary conditions at the bottom plate instead of constant temperature boundary conditions. Even at these very high Ra, both the thermal and kinetic boundary layer thicknesses obey Prandtl–Blasius scaling.

Key words: Bénard convection, turbulence simulation, turbulent convection

1. Introduction

In Rayleigh–Bénard (RB) convection, fluid in a box is heated from below and cooled from above (Ahlers, Grossmann & Lohse 2009*c*). This system is paradigmatic for turbulent heat transfer, with many applications in atmospheric and environmental physics, astrophysics and process technology. Its dynamics is characterized by the Rayleigh number $Ra = \beta g \Delta L^3/(\kappa\nu)$ and the Prandtl number $Pr = \nu/\kappa$. Here, L is the height of the sample, β is the thermal expansion coefficient, g the gravitational acceleration, Δ the temperature difference between the bottom and the top of the sample, and ν and κ the kinematic viscosity and the thermal diffusivity, respectively. Almost all experimental and numerical results on the heat transfer, indicated by the Nusselt number Nu, agree up to $Ra \approx 2 \times 10^{11}$ (see the review of Ahlers *et al.* 2009*c*, for detailed references) and are in agreement with the description of the Grossmann–Lohse (GL) theory (Grossmann & Lohse 2000, 2001, 2002, 2004). However, for higher Ra the situation is less clear.

Most experiments for $Ra \gtrsim 2 \times 10^{11}$ are performed in samples with aspect ratios $\Gamma \equiv D/L = 1/2$ and $\Gamma = 0.23$, where D and L are the diameter and height of the sample, respectively. The majority of these experiments are performed with liquid helium near its critical point (Chavanne *et al.* 2001; Niemela *et al.* 2000, 2001;

† Email address for correspondence: r.j.a.m.stevens@tnw.utwente.nl

Niemela & Sreenivasan 2006; Roche *et al.* 2001, 2002, 2010). While Niemela *et al.* (2000, 2001) and Niemela & Sreenivasan (2006) found a Nu increase with $Nu \propto Ra^{0.32}$, the experiments by Chavanne *et al.* (2001) and Roche *et al.* (2001, 2002, 2010) gave a steep Nu increase with $Nu \propto Ra^{0.38}$. In these helium experiments the Pr number increases with increasing Ra. Funfschilling, Bodenschatz & Ahlers (2009) and Ahlers *et al.* (2009*a*) and Ahlers, Funfschilling & Bodenschatz (2009*b*) performed measurements around room temperature with highly pressurized gases with nearly constant Pr and do not find such a steep increase. Multiple states in RB were observed by Roche *et al.* (2002) who found a bimodality of Nu, with 7 % difference between the two data sets. Subsequently, Chillà *et al.* (2004) and Sun, Xi & Xia (2005) showed that a finite tilt of the sample can cause a transition between different flow states. Later Xi & Xia (2008) and Weiss & Ahlers (2011) showed that in an $\Gamma = 0.5$ sample the flow can be either in the single roll state (SRS) or the double roll state (DRS), each with a specific heat transport. Recently, Niemela & Sreenivasan (2010) found two $Nu \propto Ra^{1/3}$ branches in a $\Gamma = 1$ sample. The high Ra branch is 20 % higher than the low Ra branch. By necessity, Nu increases more steeply in the transition region. The scaling in the transition region happens to be around $Nu \propto Ra^{0.5}$. There are thus considerable differences in the heat transfer obtained in these different experiments in the high Ra regime. Very recently, Ahlers and coworkers (see Ahlers *et al.* 2009*b*; Ahlers, Funfschilling & Bodenschatz 2011) even found two different branches in *one* experiment with the steepest branch going as $Nu \propto Ra^{0.36}$. Also in the experiments of Roche *et al.* (2010) two different turbulent states were observed in a $\Gamma = 0.23$ cell and $1 \times 10^{12} \lesssim Ra \lesssim 1 \times 10^{13}$. In addition, van der Poel, Stevens & Lohse (2011) showed in two-dimensional simulations that Nu can vary up to 35 % as function Γ due to changes in the flow structure.

There is no clear explanation for this disagreement although it has been conjectured that variations of the Pr number, the use of constant temperature or a constant heat flux condition at the bottom plate, the finite conductivity of the horizontal plates and sidewall, non-Oberbeck–Boussinesq effects, i.e. the dependence of the fluid properties on the temperature, the existence of multiple turbulent states (Grossmann & Lohse 2011), and even wall roughness and temperature conditions outside the sample might play a role. Since the above differences among experiments might be induced by unavoidable technicalities in the laboratory set-ups, within this context, direct numerical simulations (DNSs) are in principle a possibility to obtain reference data that strictly adhere to the intended theoretical problem and that could be used as guidelines to interpret the experiments. This is the main motivation for the present study.

2. Numerical procedure

We start this paper with a description of the numerical procedure that is used to investigate the influence on the heat transfer for two of the issues mentioned above. First, we discuss the effect of the Pr on the heat transport in the high Ra regime. Subsequently, we discuss the difference between simulations performed with a constant temperature at the bottom plate with simulations with a constant heat flux at the bottom plate. We take the constant heat flux condition only at the bottom plate, because in real setups the bottom plate is in contact with a heater while the top plate is connected to a thermostatic bath. Thus, the condition of constant heat flux applies at most only to the bottom plate (Niemela *et al.* 2000, 2001; Niemela & Sreenivasan 2006). At the top plate constant temperature boundary conditions are assumed to

strictly hold, i.e. perfect heat transfer to the recirculating cooling liquid. We conclude the paper with a brief summary, discussion, and outlook to future simulations.

The flow is solved by numerically integrating the three-dimensional Navier–Stokes equations within the Boussinesq approximation. The numerical method has already been described by Verzicco & Camussi (1997, 2003) and Verzicco & Sreenivasan (2008) and here it is sufficient to mention that the equations in cylindrical coordinates are solved by central second-order accurate finite-difference approximations in space and time. We performed simulations with constant temperature conditions at the bottom plate for $2 \times 10^7 < Ra < 1 \times 10^{12}$ and $0.5 < Pr < 10$ in an aspect ratio $\Gamma = 0.23$ sample. We also present results for a simulation at $Ra = 2 \times 10^{12}$ at $Pr = 0.7$ in a $\Gamma = 1/2$ sample. In addition, we performed simulation with a constant heat flux at the bottom plate and a constant temperature at the top plate, see Verzicco & Sreenivasan (2008) for details, for $Pr = 0.7$, $\Gamma = 1/2$, and $2 \times 10^6 \lesssim Ra \lesssim 2 \times 10^{11}$. Because in all simulations the temperature boundary conditions are assigned precisely, the surfaces are infinitely smooth, and the Boussinesq approximation is unconditionally valid, the simulations should provide a reference case for present and future experiments.

In Stevens, Verzicco & Lohse (2010*b*) we investigated the resolution criteria that should be satisfied in a fully resolved DNS and Shishkina *et al.* (2010) determined the minimal number of nodes that should be placed inside the boundary layers (BLs). The resolutions used here are based on this experience. To be sure that the flow is fully resolved we performed some simulations with a higher spatial resolution than Stevens *et al.* (2010*b*). We now performed a simulation at $Ra = 2 \times 10^{10}$ on a $769 \times 193 \times 769$ (azimuthal, radial and axial number of nodes) grid. The new result is $\sim 5\,\%$ lower than the result presented by Stevens *et al.* (2010*b*). In addition, we have increased the time averaging for the simulation at $Ra = 2 \times 10^{11}$ (Stevens *et al.* 2010*b*) with 80 dimensionless time units to 120 units in total. The result is the same as the result presented in Stevens *et al.* (2010*b*), where the simulation was run for 40 time units. For the simulation at $Ra = 2 \times 10^{12}$ we have paid special attention to the resolution in the BLs, where a sufficient spatial resolution is especially important. According to Shishkina *et al.* (2010), who assume a BL of Prandtl–Blasius type, 25 nodes in the BLs are needed for a simulation at $Ra = 2 \times 10^{12}$. Since the BL is only expected to become turbulent at $Ra \sim 10^{13}$–10^{14} at these Pr, we consider this to be a reasonable assumption. Anyhow, to be on the safer side we used 31. Whether a grid resolution has been sufficient can ultimately only be confirmed by simulations with considerably higher grid resolution, and at $Ra = 2 \times 10^{12}$ such simulations are presently not feasible.

The error bars for all simulations are based on the variation of the Nu number over time, see Stevens *et al.* (2010*b*) for details. For the simulations at $Ra = 2 \times 10^{11}$ and $Ra = 2 \times 10^{12}$ there is also some uncertainty due to possibly still slightly insufficient grid resolution, which is reflected in larger error bars below the given numerical data points as compared to those above the data points. We emphasize that Stevens *et al.* (2010*b*) showed that the simulation results are independent of the initial conditions, which suggest that long transients (Chillà *et al.* 2004) probably do not influence the results. However, we stress that the simulations at $Ra \gtrsim 10^{12}$ are not long enough to detect a possible transition between different turbulent states. Finally, we emphasize that for lower Ra (up to $Ra \approx 2 \times 10^8$) the results of our code agree well with completely independently written codes from Shishkina & Thess (2009) and Hébert *et al.* (2010) (J. Scheel, Personal communication, 2011).

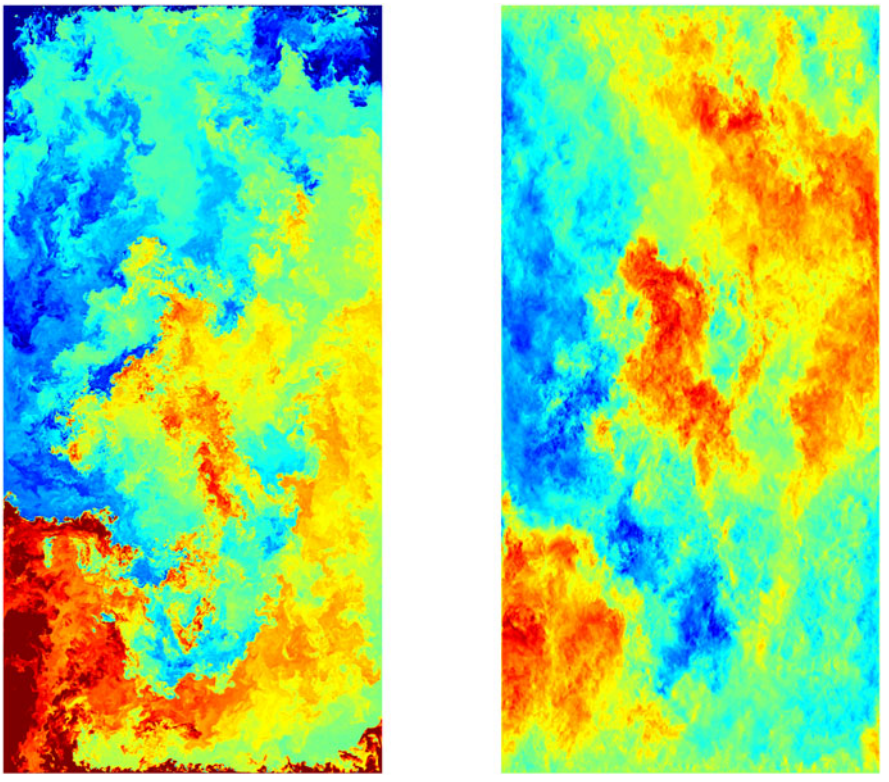

FIGURE 1. Visualization of the instantaneous temperature and temperature (left) and vertical velocity field (right) for the simulation at $Ra = 2 \times 10^{12}$ and $Pr = 0.7$ for $\Gamma = 1/2$. Red and blue indicate warm (up flowing) and cold (down flowing) fluid, respectively, in the left (right) panel. Corresponding movies can be found as supplementary material available at journals.cambridge.org/flm.

To give the reader some idea of the scale of this study we mention the resolutions that were used in the most demanding simulations, i.e. simulations that take at least 100 000 DEISA CPU (central processing unit) hours each. For $\Gamma = 0.23$ these are the simulations at $Ra = 2 \times 10^{11}$, which are performed on either a $641 \times 185 \times 1281$ grid for $Pr = 0.7$ and $Pr = 2.0$ or on a $769 \times 257 \times 1537$ grid for $Pr = 4.38$ and $Pr = 6.4$. The simulations at $Ra = 1 \times 10^{12}$ are performed on a $1081 \times 301 \times 2049$ grid. The simulations for $Ra = 2 \times 10^{11}$ were run for at least 100 dimensionless time units when time is scaled by $L/\sqrt{\beta g \Delta L}$, while the simulations at $Ra = 1 \times 10^{12}$ cover $\sim$30–40 time units. The simulation with a constant heat flux condition at the bottom plate and constant temperature condition at the top plate in a $\Gamma = 1/2$ sample with $Pr = 0.7$ at $Ra = 2.37 \times 10^{11}$ is performed on a $1081 \times 351 \times 1301$ grid. The simulation at $Ra = 2 \times 10^{12}$ with $Pr = 0.7$ in the $\Gamma = 1/2$ sample has been performed on a $2701 \times 671 \times 2501$ grid, which makes it the largest fully bounded turbulent flow simulation ever. This simulation takes about 50 000 vectorial CPU hours on HLRS (equivalent to $\approx 5 \times 10^6$ DEISA CPU hours). To store one snapshot of the field (T, u_1, u_3, because u_2 follows from continuity) requires 160 GB in binary format. A snapshot of this flow is shown in figure 1. Movies of this simulation are available as supplementary material at journals.cambridge.org/flm.

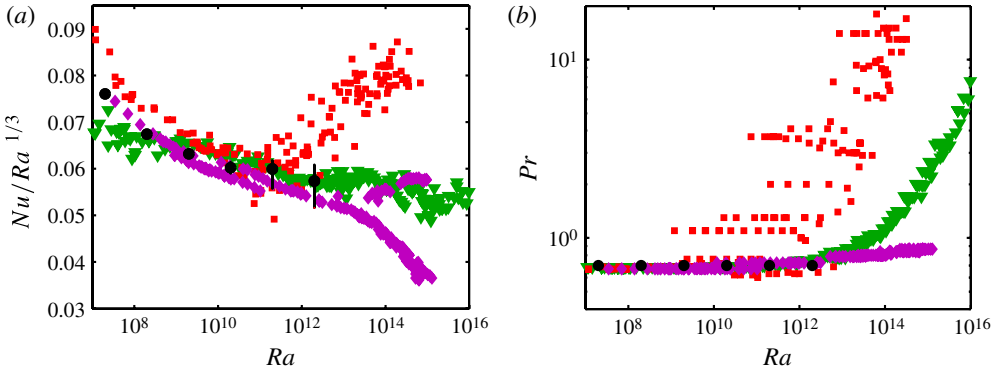

FIGURE 2. (Colour online available at journals.cambridge.org/flm) (*a*) Plot of *Nu* versus *Ra* for $\Gamma = 1/2$. The green downward pointing triangles are experimental data from Niemela *et al.* (2000, 2001) after a reanalysis reported in Niemela & Sreenivasan (2006), the red squares are from Chavanne *et al.* (2001), the purple diamonds are from Funfschilling *et al.* (2009), Ahlers *et al.* (2009*a*,*b*) and Ahlers *et al.* (2011). The DNS results for $Pr = 0.7$ are indicated in black and are from Stevens *et al.* (2010*b*). The data point for $Ra \gtrsim 2 \times 10^{10}$ are from this study. When the vertical error bar is not visible the error is smaller than the dot size. (*b*) Parameter space for the data presented in panel (*a*). Symbols as in panel (*a*).

3. Numerical results for $Nu(Ra, Pr, \Gamma)$

In figures 2(*a*) and 3(*a*) the DNS results for $Pr = 0.7$ in the $\Gamma = 0.23$ and $\Gamma = 1/2$ samples with constant temperature boundary conditions at both plates are compared with experimental data. The result for $Ra = 2 \times 10^{12}$ in the $\Gamma = 1/2$ sample agrees well with the experimental data of Niemela *et al.* (2000, 2001), Niemela & Sreenivasan (2006), Funfschilling *et al.* (2009) and Ahlers *et al.* (2009*a*,*b*), while there is a visible difference with the trend shown by the results of Chavanne *et al.* (2001). A comparison of the results for $\Gamma = 0.23$ with the experimental data of Roche *et al.* (2010) shows that there is a good agreement at $Ra = 10^{12}$ between the simulation results and the upper branch of the experimental results. However, at this *Ra* a strong disagreement with the lower experimental branch that starts around $Ra = 10^{12}$ is found. For lower *Ra*, where the lower experimental branch is not observed, we obtain a slightly larger *Nu* than in the experiments. We again stress that we performed resolution checks for this $\Gamma = 0.23$ case (up to $Ra = 2 \times 10^{10}$), and in addition considering the good agreement with the results for $\Gamma = 1/2$, we exclude that our DNS results overestimate *Nu*.

Figures 2(*b*) and 3(*b*) show that in some experiments the *Pr* number increases with increasing *Ra*. Figure 4 shows the *Nu* number as function of *Pr* for different *Ra*. This difference in *Pr* is often mentioned as one of the possible causes for the observed differences in the heat transfer between the experiments (Niemela & Sreenivasan 2003). This figure shows that the effect of the *Pr* number on the heat transfer decreases with increasing *Ra*. This means that the differences in the heat transport that are observed between the experiments for $Ra \gtrsim 10^{11}$, see figures 2(*a*) and 3(*a*), are not a *Pr* number effect. We note that Ahlers & Xu (2001) and Xia, Lam & Zhou (2002) had already experimentally measured the influence of *Pr* on the heat transfer for $Ra \lesssim 10^{11}$. However, the differences in the heat transport measurements between different experiments only become visible for $Ra \gtrsim 2 \times 10^{11}$. Therefore, the possible influence of the *Pr* was still discussed by some authors (Niemela & Sreenivasan 2003).

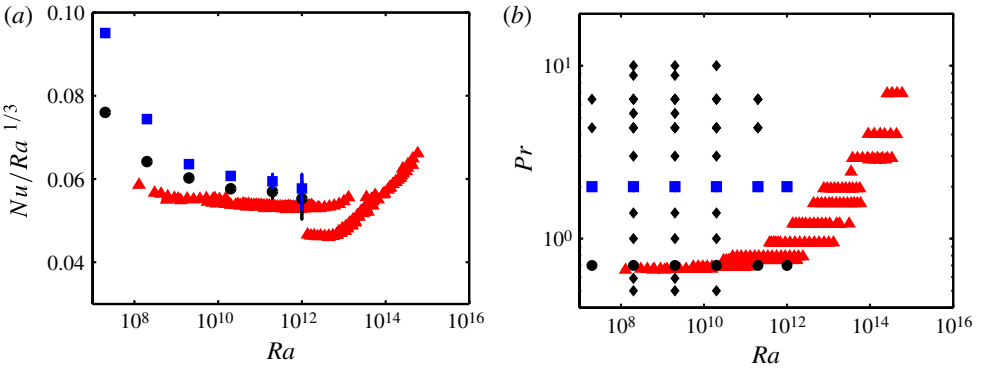

FIGURE 3. (Colour online) (*a*) Plot of Nu versus Ra for $\Gamma = 0.23$. The upward pointing red triangles are from Roche *et al.* (2010). The DNS results for $Pr = 0.7$ and $Pr = 2.0$ are indicated as black circles and blue squares, respectively. When the vertical error bar is not visible the error is smaller than the dot size. (*b*) Parameter space for the data presented in panel (*a*). Symbols as in panel (*a*). The black diamonds indicate DNS presented in this paper.

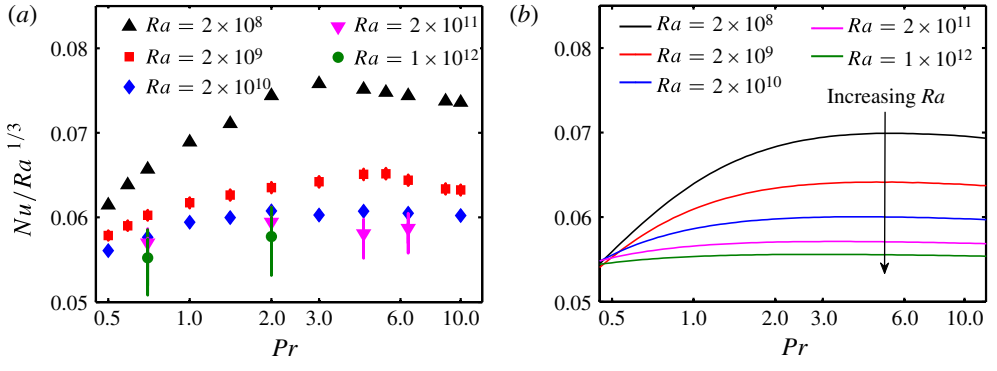

FIGURE 4. (Colour online) Plot of Nu versus Pr. The results for $Ra = 2 \times 10^8$, $Ra = 2 \times 10^9$, $Ra = 2 \times 10^{10}$, $Ra = 2 \times 10^{11}$ and $Ra = 10^{12}$ are indicated as shown in the legend. Panel (*a*) gives the DNS results for $\Gamma = 0.23$ and panel (*b*) the prediction from the GL model for $\Gamma = 1$. Here the arrow indicates the direction of increasing Ra. The slight decrease of Nu for $Pr \geqslant 3$ and not too large Ra is also seen in experiment of Ahlers & Xu (2001) and Xia *et al.* (2002).

Our simulation results now show, in agreement with the theoretical prediction of the GL-model for $\Gamma = 1$ (see figure 4), that also for $10^{11} \lesssim Ra \lesssim 10^{12}$ no significant Pr dependence is observed.

4. Scaling of thermal and kinetic boundary layers

We determined the thermal and kinetic BL thickness for the simulations in the $\Gamma = 0.23$ and $\Gamma = 1/2$ sample. The horizontally averaged thermal BL thickness (λ_θ) is determined from $\lambda_\theta^{sl}(r)$, where $\lambda_\theta^{sl}(r)$ is the intersection point between the linear extrapolation of the temperature gradient at the plate with the behaviour found in the bulk (Stevens, Clercx & Lohse 2010*a*). In figures 5(*a*) and 6(*a*) it is shown that the scaling of the thermal BL thickness is consistent with the Nu number measurements when the horizontal average is taken over the entire plate.

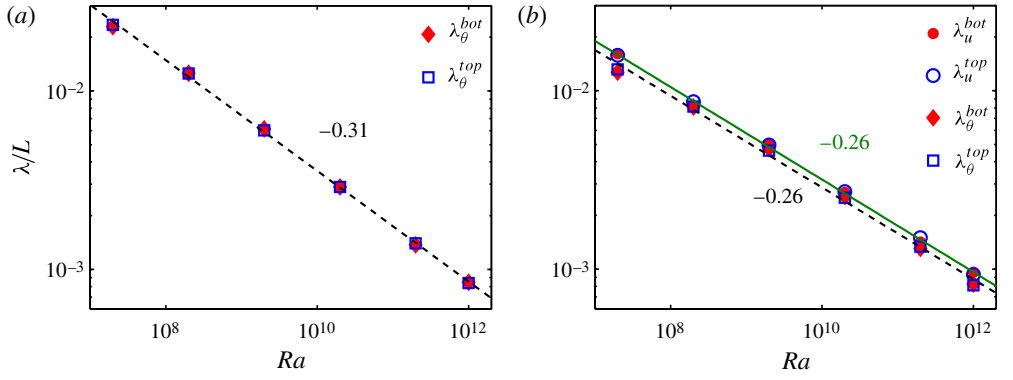

FIGURE 5. (Colour online) BL thicknesses for $Pr = 0.7$ in the $\Gamma = 0.23$ sample. (*a*) The thermal BL thickness close to the bottom and top plate averaged over the entire horizontal area scales with $Ra^{-0.31}$ (black dashed line). (*b*) The kinetic (dark green solid line) and thermal (black dashed line) BL thicknesses averaged between $0.25D/2 < r < 0.50D/2$ scale with $Ra^{-0.26}$. Note that this is slightly less than in figure 5(*a*), when we average λ_θ over the full area.

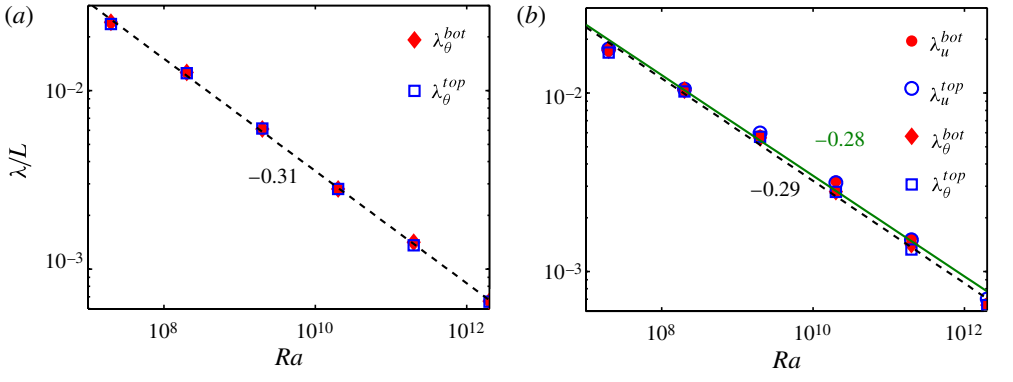

FIGURE 6. (Colour online) BL thicknesses for $Pr = 0.7$ in the $\Gamma = 1/2$ sample. (*a*) The thermal BL thickness close to the bottom and top plate averaged over the entire horizontal area scales with $Ra^{-0.31}$ (black dashed line). (*b*) The kinetic (dark green solid line/grey in print) and thermal (black dashed line) BL thicknesses averaged between $0.25D/2 < r < 0.50D/2$ scale with $Ra^{-0.28}$ and $Ra^{-0.29}$, respectively. Note that this is slightly less than in figure 6(*a*), when we average λ_θ over the full area.

The horizontally averaged kinetic BL thickness (λ_u) is determined from $\lambda_u''(r)$, where $\lambda_u''(r)$ is based on the position where the quantity $\epsilon_u'' := \boldsymbol{u} \cdot \nabla^2 \boldsymbol{u}$ reaches its maximum. We use this quantity as Stevens *et al.* (2010*b*) and Shishkina *et al.* (2010) showed that it represents the kinetic BL thickness better than other available methods. Stevens *et al.* (2010*a*,*b*) also explained that this quantity cannot be used close to the sidewall as here it misrepresents the kinetic BL thickness. For numerical reasons, it also cannot be calculated accurately in the centre region. To be on the safe side we horizontally average the kinetic BL between $0.25D/2 < r < 0.50D/2$, where D indicates the diameter of the cell and all given values were obtained over that interval, unless indicated otherwise. Figures 5(*b*) and 6(*b*) reveal that for $Pr = 0.7$ the kinetic and

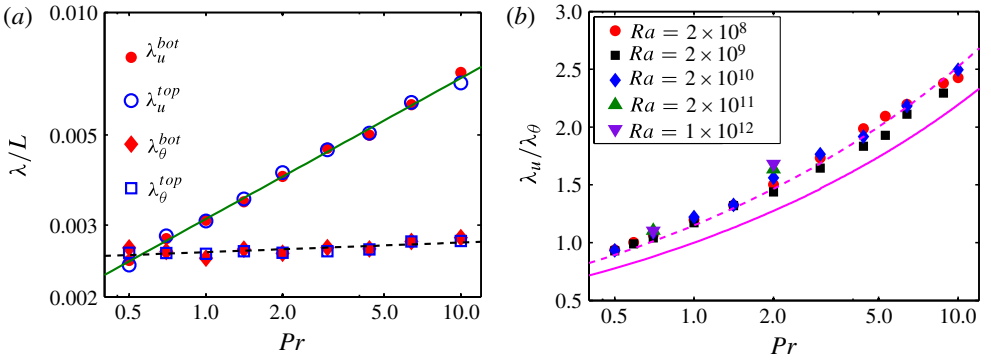

FIGURE 7. (Colour online) (*a*) Kinetic and thermal BL thicknesses close to the bottom and top plate for $Ra = 2 \times 10^{10}$ in the $\Gamma = 0.23$ sample. (*b*) The ratio between the kinetic and thermal BL thickness as function of Pr for different Ra in the $\Gamma = 0.23$ sample. The magenta solid line indicates the prediction from the Prandtl–Blasius theory (Shishkina *et al.* 2010). The magenta dashed line (grey in print), which lies 15 % above the theoretical prediction, is a guide to the eye. All numerical data are horizontally averaged for $0.25D/2 < r < 0.50D/2$.

thermal BL thickness have the same scaling and thickness as the thermal BL over a wide range of Ra in the $\Gamma = 0.23$ and $\Gamma = 1/2$ sample.

Figure 7(*a*) shows that in the $\Gamma = 0.23$ sample the thickness of the thermal BL thickness is approximately constant for $0.5 < Pr < 10$, while the kinetic BL thickness varies strongly. In figure 7(*b*) the ratio λ_u/λ_θ is compared with results of the Prandtl–Blasius BL theory. We find a *constant* difference of $\sim$15 % between the numerical results and the theoretical PB type prediction, see e.g. Shishkina *et al.* (2010). We emphasize that the deviation of the prefactor of only 15 % is remarkably small, given that the PB boundary layer theory has been developed for parallel flow over an infinite flat plate, whereas here in the aspect ratio $\Gamma = 0.23$ cell one can hardly find such regions of parallel flows at the top and bottom plates. Nonetheless, the scaling and even the ratio of the kinetic and thermal BL thicknesses for these large Ra numbers is well described by Prandtl–Blasius BL theory. We note that for $Pr = 2$ the difference between the measured λ_u/λ_θ and the theoretical predication seems to increase slightly with increasing Ra. Because this variation is absent in the $Pr = 0.7$ data we assume that this variation is due to the limited statistical data that are available as the kinetic BL thickness can only be determined in a small region. We thus do not see any indication that the BLs become turbulent for $Ra \lesssim 10^{12}$. This result agrees with the experimental results of Qiu & Xia (1998) and Sun, Cheung & Xia (2008). Indeed, Qiu & Xia (1998) showed that the kinetic BL near the sidewall obeys the scaling law of the Prandtl–Blasius laminar BL and Sun *et al.* (2008) showed the same for the BLs near the bottom plate. Recently, Zhou & Xia (2010) and Zhou *et al.* (2010) have developed a method of expressing velocity profiles in the time-dependent BL frame and found that not only does the scaling obey the PB expectation, but even the rescaled velocity and temperature profiles.

5. Constant temperature versus constant heat flux condition at the bottom plate

It has also been argued by Verzicco & Sreenivasan (2008) that the different boundary conditions at the bottom plate, i.e. that some experiments are closer to

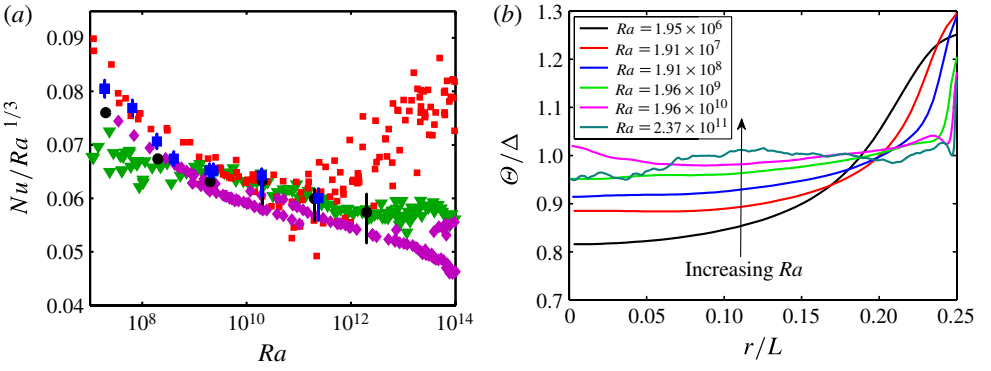

FIGURE 8. (Colour online) (*a*) Plot of Nu versus Ra for $\Gamma = 1/2$. Data as in figure 2(*a*). The numerical data for $Pr = 0.7$ with constant heat flux at the bottom and constant temperature at the top plate are indicted as blue squares and the numerical data with constant temperature condition at both plates as black circles. To make a fair comparison between both cases only simulations performed on identical grids are included in this figure. (*b*) Time-averaged temperature Θ/Δ at the bottom plate for simulations with constant heat flux at the bottom plate and constant temperature at the top plate. Here Δ is the average temperature difference between the two plates. The arrow indicates the direction of increasing Ra.

a constant temperature boundary condition, and some are closer to a constant heat flux boundary condition, might explain the differences in the heat transport that are observed in the high Ra regime. Figure 8(*a*) compares the Nu in the simulations with constant temperature and constant heat flux at the bottom plate. We emphasize that we only compare simulation results that are obtained on identical grids in order to rule out resolution effects as much as possible. In the simulations with a constant heat flux at the bottom plate we calculate the Nu number from the average heat flux at the bottom and top plate. The error bars for these simulations are larger than for the simulations with a constant temperature condition at both plates because it takes more time to reach the statically stationary state. Figure 8(*a*) shows that the difference between these two cases is small and even decreases with increasing Ra. For $Ra \gtrsim 10^{10}$ we see no difference within the (statistical) error bars.

Figure 8(*b*) reveals the time-averaged temperature of the bottom plate in the simulations with constant heat flux at the bottom plate for different Ra. The radial dependence at the lower Ra can be understood from the flow structure in the sample: due to the large-scale circulation the fluid velocities are largest in the middle of the sample. Thus, in the middle more heat can be extracted from the plate than close to the sidewall where the fluid velocities are smaller. It is the lack of any wind in the corners of the sample that causes the relatively high time-averaged plate temperature there. The figure also shows that this effect decreases with increasing Ra. The reason for this is that the turbulence becomes stronger at higher Ra and this leads to smaller flow structures. Therefore, the region close to the sidewall with relative small fluid velocities decreases with increasing Ra and this leads to a more uniform plate temperature at higher Ra. In figure 9 we show the profiles of the root mean square (r.m.s.) temperature fluctuations horizontally averaged over $0 < r < 0.75D/2$. All profiles are normalized with the time-averaged temperature difference Δ between the two plates. The r.m.s. temperature fluctuation profiles near the top plate show a sharp peak, see figure 9(*c*), before they obviously drop to zero at the top plate, where the temperature is assumed constant. Variation between the peak heights is visible,

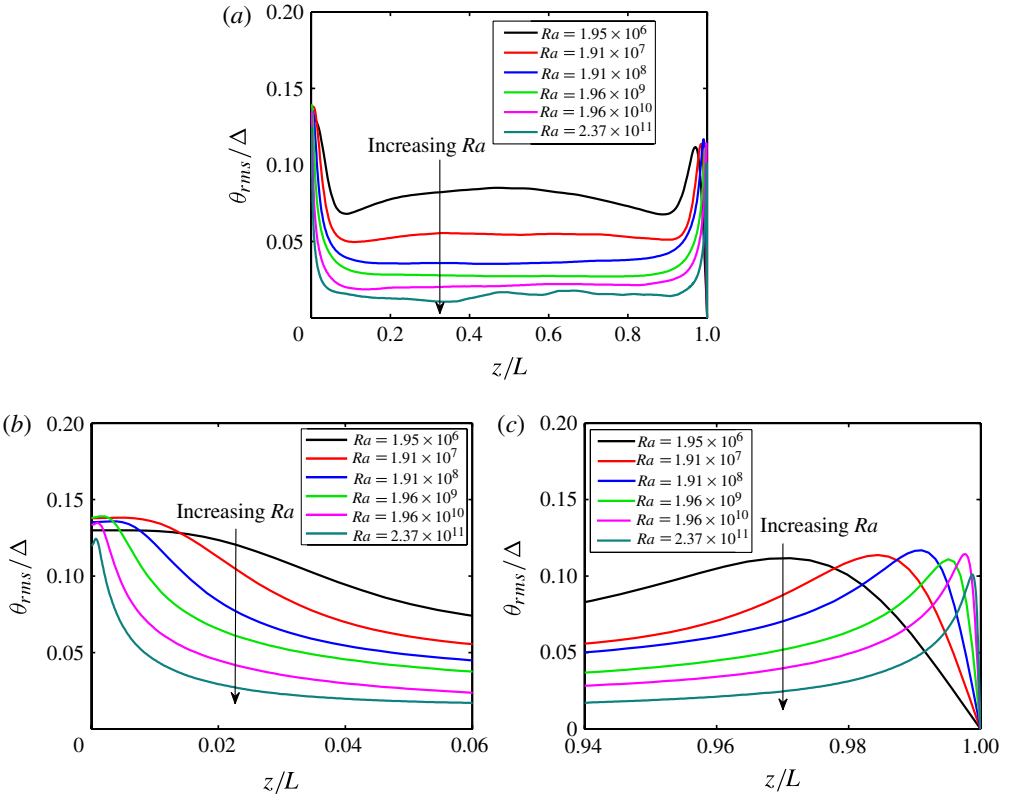

FIGURE 9. (Colour online) Normalized r.m.s. profiles of the temperature fluctuations horizontally averaged over $0 < r < 0.75D/2$. (*a*) The entire domain. (*b*) Enlargement of the area close to lower plate where a constant heat flux condition boundary condition is applied. (*c*) Enlargement of the area close to upper plate where a constant temperature boundary condition is applied. In each panel the arrow indicates the direction of increasing Ra.

because time averaging is limited. Near the bottom plate (see figure 9*b*) there is no sharp peak in the temperature fluctuation profiles, because the temperature of the bottom plate is allowed to fluctuate. Since the heat capacity of the plate is not taken into account, these temperature fluctuations are comparable with the fluctuations found in the BL. From all of this we conclude that the difference between simulation with constant temperature and constant heat flux condition at the bottom plate disappears with increasing Ra.

The small differences between the simulations with constant temperature and constant heat flux at the bottom plate show that the differences between the experiments in the high Ra number regime cannot be explained by different plate conductivity properties. This finding is in agreement with the results of Johnston & Doering (2009). In their periodic two-dimensional RB simulations the heat transfer for simulations with constant temperature and constant heat flux (both at the bottom and the top plate) becomes equal at $Ra \approx 5 \times 10^6$. For the three-dimensional simulations the heat transfer for both cases also becomes equal, but at higher Ra. This is due to the geometrical effect discussed before, see figure 8(*b*), that cannot occur in periodic two-dimensional simulations (Johnston & Doering 2009).

6. Conclusions

In summary, we have presented results from three-dimensional DNS for RB convection in cylindrical samples of aspect ratios $\Gamma = 0.23$ and $\Gamma = 1/2$ up to $Ra = 2 \times 10^{12}$ and a broad range of Pr. The simulation at $Ra = 2 \times 10^{12}$ with $Pr = 0.7$ in an aspect ratio $\Gamma = 1/2$ sample and constant temperature condition at both plates is in good agreement with the experimental results of Niemela *et al.* (2000, 2001), Niemela & Sreenivasan (2006), Funfschilling *et al.* (2009) and Ahlers *et al.* (2009*a*,*b*), while there is a visible difference in the high end of Ra with the trend shown by the results of Chavanne *et al.* (2001). In addition, we showed that the differences in the heat transfer observed between experiments for $2 \times 10^{11} \lesssim Ra \lesssim 2 \times 10^{12}$ can neither be explained by Pr number effects, nor by the assumption of constant heat flux conditions at the bottom plate instead of constant temperature conditions. We also demonstrated that the scaling of the kinetic and thermal BL thicknesses in this high Ra number regime is well described by the Prandtl–Blasius theory up to $Ra \lesssim 2 \times 10^{12}$ for $0.5 < Pr < 10$ in a $\Gamma = 0.23$ and a $\Gamma = 1/2$ sample.

Several questions remain: which effect is responsible for the observed difference in Nu versus Ra scaling in the various experiments? Are there perhaps different turbulent states in the highly turbulent regime as has been suggested for RB flow by Grossmann & Lohse (2011), but also for other turbulent flows in closed systems by Cortet *et al.* (2010)? At what Ra do the BLs become turbulent? In answering some aspects of these questions DNS will play a leading role, because both the velocity and temperate fields are known in the whole domain (including in the BLs where the transition between the states is suggested to take place), which allows for the flow structures to be studied in detail. Some three-dimensional fields are available for download in the database at the website splashdown.caspur.it.

We thank J. Niemela, K. R. Sreenivasan, G. Ahlers, and P. Roche for providing the experimental data. The presented simulations were performed on Huygens (DEISA [Distributed European Infrastructure for Supercomputing Applications] project), CASPUR (Inter-University Consortium for the Application of Super-Computing for Universities and Research) and HLRS (High Performance Computing Center Stuttgart). We gratefully acknowledge the support of Wim Rijks (SARA) and we thank the DEISA Consortium (www.deisa.eu), co-funded through the EU FP7 project RI-222919, for support within the DEISA Extreme Computing Initiative. R.J.A.M.S. was financially supported by the Foundation for Fundamental Research on Matter (FOM). We thank the Kavli institute, where part of the work has been done, for its hospitality. This research was supported in part by the National Science Foundation under grant number PHY05-51164, via the Kavli Institute of Theoretical Physics.

Supplementary movies are available at journals.cambridge.org/flm.

REFERENCES

AHLERS, G., BODENSCHATZ, E., FUNFSCHILLING, D. & HOGG, J. 2009*a* Turbulent Rayleigh–Bénard convection for a Prandtl number of 0.67. *J. Fluid Mech.* **641**, 157–167.

AHLERS, G., FUNFSCHILLING, D. & BODENSCHATZ, E. 2009*b* Transitions in heat transport by turbulent convection at Rayleigh numbers up to 10^{15}. *New J. Phys.* **11**, 123001.

AHLERS, G., FUNFSCHILLING, D. & BODENSCHATZ, E. 2011 Addendum to transitions in heat transport by turbulent convection at Rayleigh numbers up to 10^{15}. *New J. Phys.* **13**, 049401.

AHLERS, G., GROSSMANN, S. & LOHSE, D. 2009*c* Heat transfer and large scale dynamics in turbulent Rayleigh–Bénard convection. *Rev. Mod. Phys.* **81**, 503.

AHLERS, G. & XU, X. 2001 Prandtl-number dependence of heat transport in turbulent Rayleigh–Bénard convection. *Phys. Rev. Lett.* **86**, 3320–3323.

CHAVANNE, X., CHILLA, F., CHABAUD, B., CASTAING, B. & HEBRAL, B. 2001 Turbulent Rayleigh–Bénard convection in gaseous and liquid He. *Phys. Fluids* **13**, 1300–1320.

CHILLÀ, F., RASTELLO, M., CHAUMAT, S. & CASTAING, B. 2004 Long relaxation times and tilt sensitivity in Rayleigh–Bénard turbulence. *Euro. Phys. J.* B **40**, 223–227.

CORTET, P., CHIFFAUDEL, A., DAVIAUD, F. & DUBRULLE, B. 2010 Experimental evidence of a phase transition in a closed turbulent flow. *Phys. Rev. Lett.* **105**, 214501.

FUNFSCHILLING, D., BODENSCHATZ, E. & AHLERS, G. 2009 Search for the 'ultimate state' in turbulent Rayleigh–Bénard convection. *Phys. Rev. Lett.* **103**, 014503.

GROSSMANN, S. & LOHSE, D. 2000 Scaling in thermal convection: a unifying view. *J. Fluid Mech.* **407**, 27–56.

GROSSMANN, S. & LOHSE, D. 2001 Thermal convection for large Prandtl number. *Phys. Rev. Lett.* **86**, 3316–3319.

GROSSMANN, S. & LOHSE, D. 2002 Prandtl and Rayleigh number dependence of the Reynolds number in turbulent thermal convection. *Phys. Rev.* E **66**, 016305.

GROSSMANN, S. & LOHSE, D. 2004 Fluctuations in turbulent Rayleigh–Bénard convection: the role of plumes. *Phys. Fluids* **16**, 4462–4472.

GROSSMANN, S. & LOHSE, D. 2011 Multiple scaling in the ultimate regime of thermal convection. *Phys. Fluids* **23**, 045108.

HÉBERT, F., HUFSCHMID, R., SCHEEL, J. & AHLERS, G. 2010 Onset of Rayleigh–Bénard convection in cylindrical containers. *Phys. Rev.* E **81**, 046318.

JOHNSTON, H. & DOERING, C. R. 2009 Comparison of turbulent thermal convection between conditions of constant temperature and constant flux. *Phys. Rev. Lett.* **102**, 064501.

NIEMELA, J., SKRBEK, L., SREENIVASAN, K. R. & DONNELLY, R. 2000 Turbulent convection at very high Rayleigh numbers. *Nature* **404**, 837–840.

NIEMELA, J., SKRBEK, L., SREENIVASAN, K. R. & DONNELLY, R. J. 2001 The wind in confined thermal turbulence. *J. Fluid Mech.* **449**, 169–178.

NIEMELA, J. & SREENIVASAN, K. R. 2003 Confined turbulent convection. *J. Fluid Mech.* **481**, 355–384.

NIEMELA, J. & SREENIVASAN, K. R. 2006 Turbulent convection at high Rayleigh numbers and aspect ratio 4. *J. Fluid Mech.* **557**, 411–422.

NIEMELA, J. J. & SREENIVASAN, K. R. 2010 Does confined turbulent convection ever attain the 'asymptotic scaling' with 1/2 power? *New J. Phys.* **12**, 115002.

VAN DER POEL, E. P., STEVENS, R. J. A. M. & LOHSE, D. 2011 Connecting flow structures and heat flux in turbulent Rayleigh–Bénard convection, *Phys. Rev.* E. (in press).

QIU, X. L. & XIA, K.-Q. 1998 Viscous boundary layers at the sidewall of a convection cell. *Phys. Rev.* E **58**, 486–491.

ROCHE, P. E., CASTAING, B., CHABAUD, B. & HEBRAL, B. 2001 Observation of the 1/2 power law in Rayleigh–Bénard convection. *Phys. Rev.* E **63**, 045303.

ROCHE, P. E., CASTAING, B., CHABAUD, B. & HEBRAL, B. 2002 Prandtl and Rayleigh numbers dependences in Rayleigh–Bénard convection. *Europhys. Lett.* **58**, 693–698.

ROCHE, P.-E., GAUTHIER, F., KAISER, R. & SALORT, J. 2010 On the triggering of the ultimate regime of convection. *New J. Phys.* **12**, 085014.

SHISHKINA, O., STEVENS, R. J. A. M., GROSSMANN, S. & LOHSE, D. 2010 Boundary layer structure in turbulent thermal convection and its consequences for the required numerical resolution. *New J. Phys.* **12**, 075022.

SHISHKINA, O. & THESS, A. 2009 Mean temperature profiles in turbulent Rayleigh–Bénard convection of water. *J. Fluid Mech.* **633**, 449–460.

STEVENS, R. J. A. M., CLERCX, H. J. H. & LOHSE, D. 2010*a* Boundary layers in rotating weakly turbulent Rayleigh–Bénard convection. *Phys. Fluids* **22**, 085103.

STEVENS, R. J. A. M., VERZICCO, R. & LOHSE, D. 2010*b* Radial boundary layer structure and Nusselt number in Rayleigh–Bénard convection. *J. Fluid Mech.* **643**, 495–507.

SUN, C., CHEUNG, Y. H. & XIA, K. Q. 2008 Experimental studies of the viscous boundary layer properties in turbulent Rayleigh–Bénard convection. *J. Fluid Mech.* **605**, 79–113.

SUN, C., XI, H.-D. & XIA, K.-Q. 2005 Azimuthal symmetry, Flow dynamics and Heat transport in turbulent thermal convection in a cylinder with an aspect ratio of 0.5. *Phys. Rev. Lett.* **95**, 074502.

VERZICCO, R. & CAMUSSI, R. 1997 Transitional regimes of low-prandtl thermal convection in a cylindrical cell. *Phys. Fluids* **9**, 1287–1295.

VERZICCO, R. & CAMUSSI, R. 2003 Numerical experiments on strongly turbulent thermal convection in a slender cylindrical cell. *J. Fluid Mech.* **477**, 19–49.

VERZICCO, R. & SREENIVASAN, K. R. 2008 A comparison of turbulent thermal convection between conditions of constant temperature and constant heat flux. *J. Fluid Mech.* **595**, 203–219.

WEISS, S. & AHLERS, G. 2011 Turbulent Rayleigh–Bénard convection in a cylindrical container with aspect ratio $\Gamma = 0.5$ and Prandtl number $Pr = 4.38$. *J. Fluid Mech.* **676**, 5–40.

XI, H.-D. & XIA, K.-Q. 2008 Flow mode transitions in turbulent thermal convection. *Phys. Fluids* **20**, 055104.

XIA, K.-Q., LAM, S. & ZHOU, S. Q. 2002 Heat-flux measurement in high-Prandtl-number turbulent Rayleigh–Bénard convection. *Phys. Rev. Lett.* **88**, 064501.

ZHOU, Q., STEVENS, R. J. A. M., SUGIYAMA, K., GROSSMANN, S., LOHSE, D. & XIA, K.-Q. 2010 Prandtl–Blasius temperature and velocity boundary layer profiles in turbulent Rayleigh–Bénard convection. *J. Fluid Mech.* **664**, 297–312.

ZHOU, Q. & XIA, K.-Q. 2010 Measured instantaneous viscous boundary layer in turbulent Rayleigh–Bénard convection. *Phys. Rev. Lett.* **104**, 104301.